PHYSICAL REVIEW C **111**, 014322 (2025)

Evidence for shape transitions near ^{189}W through direct mass measurements

M. Mukai,[1] Y. Hirayama,[1] P. Schury,[1] Y. X. Watanabe,[1] T. Hashimoto,[2] N. Hinohara,[3] S. C. Jeong,[1]
H. Miyatake,[1] J. Y. Moon,[2] T. Niwase,[4] M. Reponen,[5] M. Rosenbusch,[6] H. Ueno,[6] and M. Wada[1]
[1]*Wako Nuclear Science Center, Institute of Particle and Nuclear Studies,*
High Energy Accelerator Research Organization (KEK), Wako, Saitama 351-0198, Japan
[2]*Institute for Basic Science, 55 Expo-ro, Yuseong-gu, Daejeon 34126, Korea*
[3]*Center for Computational Sciences, University of Tsukuba, Tsukuba 305-8577, Japan*
[4]*Department of Physics, Kyushu University, 744 Motooka, Nishi-ku, Fukuoka 819-0395, Japan*
[5]*Department of Physics, University of Jyväskylä, PO Box 35 (YFL), FI-40014 Jyväskylä, Finland*
[6]*RIKEN Nishina Center for Accelerator-Based Science, Wako, Saitama 351-0198, Japan*

(Received 8 August 2024; accepted 19 December 2024; published 17 January 2025)

Precise mass measurements of refractory nuclei produced by multinucleon transfer reactions of a ^{136}Xe beam and $^{\mathrm{nat}}$Ir target were conducted at the KISS (KEK Isotope Separation System) facility, using a multireflection time-of-flight mass spectrograph. The study encompasses ions with mass numbers $A = 188$, 189, 190, 192, and atomic numbers $Z = 74$–79. Our findings show good agreement between the evaluated masses, excluding ^{192}Re, and known values, within the specified error margins. The assessment includes the reevaluation of the rejected mass value for ^{189}W in the AME2020 atomic mass evaluation. The determined atomic mass of ^{189}W aligns closely with previously reported values obtained through direct mass measurements using the GSI storage ring ESR and β-decay Q-value measurements. The flat S_{2n} pattern between ^{189}W and ^{190}W was interpreted as a result of a shape transition at $N = 116$ according to Hartree-Fock-Bogoliubov calculations with the SV-min parametrization. Additionally, the updated mass value for ^{192}Re also suggests a shape transition at $N = 117$, consistent with previous studies.

DOI: 10.1103/PhysRevC.111.014322

I. INTRODUCTION

The mass of a nucleus is a fundamental bulk property, inherently reflecting the strong interaction within the nucleus. Systematic variations in mass values along isotopic chains provide profound insights into nuclear structure, revealing changes in binding energy and the influence of shell structure. This information is crucial for understanding the properties and stability of nuclei at specific neutron and proton numbers. Moreover, the mass values of atomic nuclei are crucial data not only for understanding the laws of physics in the nucleus but also for unraveling the processes of element synthesis in celestial phenomena [1,2]. In recent years, an increasing number of precision measurements of the masses of various unstable nuclei have been accomplished using a variety of direct methods, including time-of-flight (TOF) [3–5], revolution frequency [6], and cyclotron frequency [7] measurements. Nevertheless, when measured mass values deviate significantly from predicted values in the Atomic Mass Evaluation (AME) [8] or depart from a smooth trend, further validation through complementary methods becomes imperative.

The mass value of ^{189}W shown in AME2016 [9] is based on the Q_β measurement [10] and Schottky mass spectroscopy using the GSI storage ring ESR [11]. The atomic mass values, assessed with a precision of 0.2 ppm, reveal a distinct trend in two-neutron separation energy for ^{190}W. This observed behavior is attributed to a larger contribution from the collective component suggested by the interacting boson approximation (IBA) model [11], resulting in an increased binding energy. The observed S_{2n} trend for W differs from that seen in Os isotopes with two more protons, becoming flat from ^{189}W onwards. Due to the observed nonsmooth trends at ^{189}W, the previous experimental mass values for ^{189}W were rejected in AME2020.

Using a multireflection time-of-flight mass spectrograph (MRTOF-MS) at the KISS facility, we conducted mass measurements of nuclides produced through the multinucleon transfer reaction $^{136}\mathrm{Xe} + {}^{\mathrm{nat}}\mathrm{Ir}$. In this paper, we report the atomic mass values for nuclei with atomic mass numbers $A = 188,\ 189,\ 190$, and 192, including ^{189}W.

II. EXPERIMENT

The experiment was performed at the KISS facility [12–14] constructed at the RIKEN Nishina Center. The nuclei were produced in multinucleon transfer reactions using a beam of ^{136}Xe at 10.75 MeV/nucleon impinging upon a natural iridium target (10 μm in thickness).

The reaction products were thermalized and neutralized in a doughnut-shaped argon gas cell pressurized to about 80 kPa at room temperature [14]. The production yields of neutron-rich W and Re isotopes are significantly less than nuclei nearer to the stable ^{191,193}Ir isotopes. Therefore, two-step laser resonance ionization was employed at the gas cell exit to enhance the extraction yields of the more exotic isotopes.

The excitation transitions from the atomic ground state of W and Re were $5d^46s^2\ {}^5D_0 \rightarrow 5d^5({}^4D)6s\ 1^\circ$ ($\lambda_1 = 260.717$ nm) [15] and $5d^56s^2\ {}^6S_{5/2} \rightarrow 5d^46s^2({}^5D)6p\ 5/2^\circ$ ($\lambda_1 = 252.076$ nm) [16], respectively. The first-step laser wavelengths were obtained from a dye laser (Radiant Dyes, NarrowScan) equipped with a frequency conversion unit, by using a dye solution of Coumarin 500. The dye laser was pumped by an excimer laser (XeCl, 307.9 nm, Lambda Physik, LPX240i). The ionization of excited atoms was achieved by using $\lambda_2 = 308$ nm radiation obtained from a second excimer laser. The two excimer lasers were synchronized, with a repetition rate of 50 Hz for the ionization. The typical laser powers at the entrance of the gas cell were about 75 μJ/pulse for the first-step laser and 25 mJ/pulse for the second-step laser.

The ions extracted from the gas cell were efficiently transported, typically with an efficiency of over 90%, into a high-vacuum region using a triplet of multipole radiofrequency (RF) ion guides, and then electrostatically accelerated to an energy of 20 keV. The mass-to-charge ratio (A/q) of the transported ions was selected by using a dipole magnet with a mass resolving power of $A/\Delta A \approx 900$. The mass-selected ion beams were transported to a mass measurement system for precision identification of the isobars.

The mass measurement system of KISS is depicted in Fig. 2 of Ref. [17]. It consists of a windowless gas-cell-based ion cooler-buncher (GCCB), a triplet RF ion trap system, and a MRTOF-MS [18]. For high-resolution measurements in the MRTOF-MS, lowering the energy of the ion beam to form low-energy ion bunches is necessary. To this end, the ions were injected and stopped in the GCCB [19], which was filled with helium gas to a pressure of 120 Pa. During the stopping process, the ions are prone to experience electron-stripping, followed by electron capture, ending in the highest charge state with ionization potential below that of helium. The ionic charge of elements around Ir tended toward $q = 2$ there due to the higher first ionization potential of the He atom [20]. The thermalized ions were pushed toward an RF-carpet (RFC) [21] at the end of the GCCB by an electric field gradient generated from a "DC cylinder" which was composed of a series of thin ring electrodes printed on a polyimide foil and connected with a resistor network. The ions were efficiently transported to an exit hole at the center of the RFC by the combination of a 44 kHz audio frequency signal applied 90 degree out of phase between adjacent electrodes superimposed on a repelling RF potential [22] of 7.8 MHz signals applied 180 degrees out of phase between adjacent electrodes. A quadrupole RF ion guide was used to transport ions into the trap system, which had higher vacuum pressure.

The trap system consists of two linear Paul traps and a "flat trap" [23]. The linear Paul traps are located on each side of the flat trap, allowing separate and simultaneous accumulation of reference and analyte ions. One is for the accumulation of analyte ions extracted from the GCCB, and the other is for accumulation of the reference ions (^{85}Rb$^+$) from an alkali ion source. The ions from each side were transferred to the flat trap alternatively every 25 ms. The ions were cooled down to less than 1 eV in the flat trap by the dilute helium buffer gas (He, 99.9999%), and then ejected toward the MRTOF-MS through a pin hole in the flat trap's central electrode by inducing a dipole electric field in the center of the flat trap.

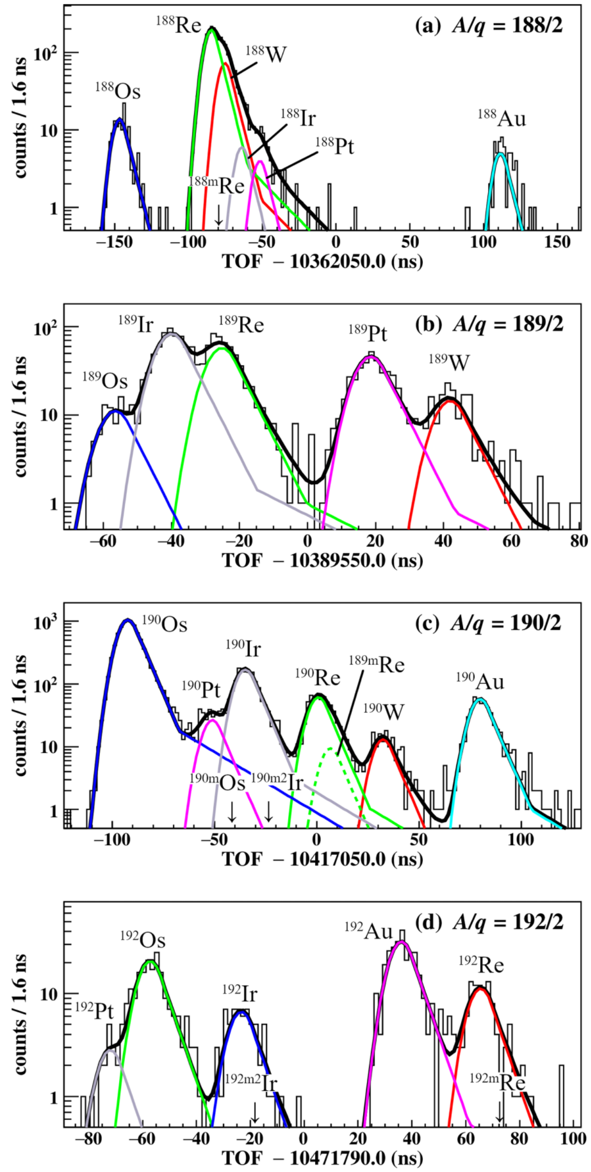

FIG. 1. Measured TOF spectra of $A/q = 188/2$, 189/2, 190/2, and 192/2 ions. The colored curves show the best fitting curves to the data. The black line represents the sum of the entire peak distribution included in the TOF spectrum. The positions of TOF of ground and isomeric states considered in the fitting but not appearing in the best fitting results are shown by downward black arrows with labels.

After being captured in the MRTOF-MS, the ions traveled between a pair of electrostatic ion mirrors, back and forth 603 times with a flight time of ≈ 10 ms. The ions were detected by an electron multiplier ion detector (MagneTOF Mini, ETP Ion Detect Pty. Ltd.) after ejection from the MRTOF-MS. The overall efficiency of the mass measurement system, from the GCCB to the ion detector with a lap number of 603 in the MRTOF, was measured to be about 2%, and typical mass

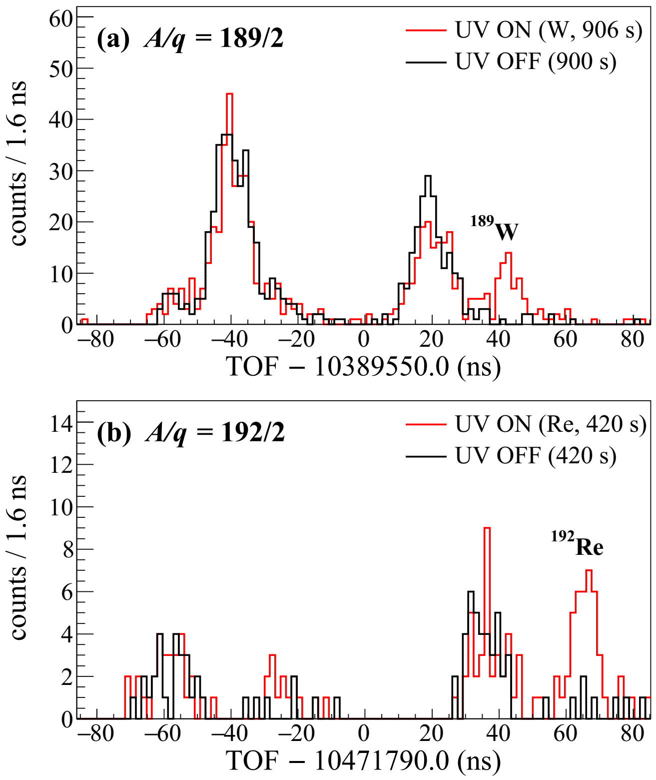

FIG. 2. Measured TOF spectra of (a) $A/q = 189/2$ and (b) $A/q = 192/2$ ions with UV (λ_1) on and off for resonant ionization of ^{189}W and ^{192}Re.

resolving power was $m/\Delta m \approx 4 \times 10^5$. The TOF values of reference ^{85}Rb$^+$ ions were utilized to correct for drift in the TOF and the calculation of a constant time offset t_0 as explained in the next section [24].

The mass measurement was conducted for $A/q = 188/2$, $189/2$, $190/2$, and $192/2$ ions; the $A/q = 191/2$ and $193/2$ ions were excluded from study due to the dominating intensity of the target material nuclides. All measured TOF spectra are shown in Fig. 1. In addition to laser ionized W and Re ions, we observed intense isobaric contaminants. As their rate was independent of the voltage applied to ion suppression electrodes near the gas cell exit, they might be ionized in the RF ion guides due to the high radiation environment induced by the primary beam irradiation. Figure 2 shows typical TOF spectra measured with and without the laser ionization for ^{189}W and ^{192}Re. We confirmed that ion count rates were clearly enhanced more than ten times by laser resonance ionization whereas the contaminant ion counts were independent, further supporting the idea that these contaminants are created by the primary beam induced radiation.

III. ANALYSIS

A drift of TOF can occur due to the changes of electric fields by thermal expansion of the components in the MRTOF-MS [24,25]. To ameliorate this effect, all acquired TOF spectra obtained in the experiment were analyzed after drift correction, enabling the determination of the TOF for each isotope. To simplify analysis, the drift correction was performed in a manner that maintained the reference ion TOF at the value determined in the first minutes of the measurements. Each spectrum was divided into a series of subspectra including 200 events of reference ions, and the ^{85}Rb$^+$ spectral peak was fitted. The TOF of each ion in the ith sub-spectra was multiplied by the factor t_1/t_i, where t_i is the fitted TOF of the reference ions in the ith subspectrum and t_1 is the fitted TOF of the reference ions in the first subspectrum of the first measurement of the experiment. The TOF spectra shown in Figs. 1 and 2 are the spectra after the drift correction. The following fitting analysis was applied to determine the TOF value of each ion species.

The TOF distribution of a single ion species exhibits asymmetric shapes with tails extending towards later flight times. This is attributed to higher-order optical aberrations in the electrostatic mirrors and low-angle scattering from residual gas during flight [26]. To describe the asymmetric shape, a Gaussian-exponential hybrid function with two exponential tails on later side was employed. The first exponential tail starts at the switching point of $t_1 = t_{\text{peak}} + \sigma$, and the extended second tail appears at $t_2 = t_{\text{peak}} + \sigma + \Delta t$, where σ is the standard deviation of the Gaussian and Δt is the time interval between t_1 and t_2:

$$f(t) = \text{Amplitude} \times \begin{cases} e^{-(t-t_{\text{peak}})^2/(2\sigma^2)} & \text{for } t < t_1, \\ e^{-(t-t_1)/\tau_1 - 1/2} & \text{for } t_1 \leqslant t < t_2, \\ e^{-(t-t_2)/\tau_2 - 1/2 - \Delta t/\tau_1} & \text{for } t \geqslant t_2. \end{cases} \tag{1}$$

Here, t_{peak} denotes the position of the fit function's maximum, and τ_i ($i = 1$ or 2) signifies the slope of the first or second exponential tail. The fitting analysis aimed to minimize the chi-squared value was carried out using the ROOT [27] framework and the MINUIT library [28] for function minimization and error analysis.

In the fitting process, we considered the presence of all potentially extractable isotopes, including isomers with half-lives exceeding 0.5 seconds, taking into account the typical extraction time of ions from the gas cell. However, isomers with low excitation energies below 60 keV, such as $^{189\text{m}}$Os ($E_{\text{x}} = 30.82(2)$ keV, $T_{1/2} = 5.81(10)$ h [29]), $^{190\text{m}1}$Ir ($E_{\text{x}} = 26.1(1)$ keV, $T_{1/2} = 1.120(3)$ h [30]), and $^{192\text{m}1}$Ir ($E_{\text{x}} = 56.720(5)$ keV, $T_{1/2} = 1.45(5)$ min [31]), were not considered because the analysis lacked sensitivity, resulting from insufficient mass resolving power. The excitation energy of the isomer was constrained within the range of the uncertainties indicated in the Nuclear Data Sheets. To fit the spectra with the same response function, the spectra for $A/q = 188/2$, $189/2$, $190/2$, and $192/2$ ions were simultaneously fitted with shared shape-related parameters.

Using the peak positions (t_{peak}) obtained from the fitting, the atomic mass values (m) were calculated using the following equation:

$$m = \frac{q}{q_{\text{ref}}}(m_{\text{ref}} - q_{\text{ref}} m_e)\rho^2 + q m_e, \qquad \rho = \frac{t_{\text{peak}} - t_0}{t_{\text{ref}} - t_0}, \tag{2}$$

TABLE I. The squares of TOF ratio, ρ^2, the mass excess values, and differences of atomic mass between AME2020 and the present study. The reference nucleus for the analysis is ^{190}Os. The values for ^{188}Ir and ^{188}Pt, whose amplitudes were zero within the error margin, are not written. The error values of $m - m_{\mathrm{AME20}}$ only include the uncertainties evaluated from the fitting analysis. An asterisk (*) on a nuclide indicates that the atomic mass was determined directly for the first time in this study.

Nuclide	ρ^2	Mass excess (keV/c^2)	$m - m_{\mathrm{AME20}}$ (keV/c^2)
^{188}W*	0.989 471 21 (40)	−38 727 (71)	−59 (71)
^{188}Re*	0.989 469 44 (13)	−39 041 (23)	−24 (23)
^{188}Os	0.989 457 58 (28)	−41 139 (50)	−2 (50)
^{188}Au	0.989 506 88 (46)	−32 415 (81)	−44 (81)
^{189}W	0.994 752 72 (32)	−35 690 (56)	120 (56)
^{189}Re*	0.994 739 86 (17)	−37 964 (31)	15 (31)
^{189}Os	0.994 733 87 (39)	−39 025 (69)	−38 (69)
^{189}Ir*	0.994 737 04 (14)	−38 464 (25)	−14 (25)
^{189}Pt*	0.994 748 25 (18)	−36 481 (32)	−11 (32)
^{190}W	1.000 023 95 (34)	−34 470 (61)	−101(61)
^{190}Re*	1.000 017 87 (26)	−35 546 (47)	37 (47)
^{190}Ir	1.000 011 02 (10)	−36 757 (18)	−3 (18)
^{190}Pt	1.000 007 92 (39)	−37 307 (69)	0 (69)
^{190}Au	1.000 033 06 (14)	−32 859 (24)	−25 (24)
^{192}Re	1.010 568 08 (32)	−31 737 (56)	−148(56)
^{192}Os	1.010 544 39 (29)	−35 928 (50)	−46 (50)
^{192}Ir*	1.010 550 92 (41)	−34 772 (73)	63 (73)
^{192}Pt*	1.010 541 53 (122)	−36 434 (215)	−146(215)
^{192}Au*	1.010 562 39 (18)	−32 742 (32)	30 (32)

where m_e is the electron mass, and t_0 represents the offset in flight time due to the finite signal transmission time in the measurement system. Substituting the precisely known atomic mass values of ^{85}Rb and ^{190}Os, along with the flight times obtained from fitting, into the above equation, we determined t_0 to be 206(4) ns. For calculating the mass values of other isotopes, we used the atomic mass (m_{ref}) and flight time (t_{ref}) values of ^{190}Os as the reference.

IV. RESULTS

In Fig. 1, the curves obtained from the best-fit results of the TOF spectra are shown for each element with colored solid and dashed lines for the ground and isomeric states, respectively. As indicated by the black downward arrows, several ground and isomeric states did not appear in the best-fit results. Table I shows our values of ρ^2, derived mass excess, and deviation from AME2020 atomic mass values. Figure 3 presents a plot of the deviation from AME2020 atomic mass values for each isotope. As a result of the fit, the intensity of the small amounts of ^{188}Ir and ^{188}Pt, which strongly overlap with the tail of the abundantly produced ^{188}Re, became statistically zero within the uncertainty. Therefore, the mass values for these isotopes could not be determined and are not listed in Table I and Fig. 3.

Two mass data for ^{189}W which have been reported previously in the studies of the Q_β [10] and revolution frequency using the GSI-ESR [11] are also shown in Fig. 3 as a blue triangle and red circle, respectively. The mass values of ^{189}W obtained from the three measurements are in good agreement within their respective uncertainties. Figure 4 shows the plot of two-neutron separation energy (S_{2n}) of even-Z nuclei in the vicinity of W, where S_{2n} is defined as:

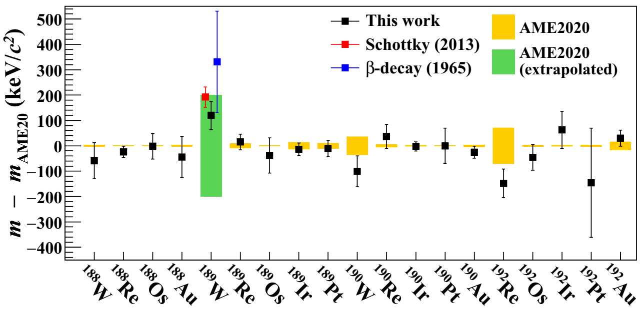

FIG. 3. Mass difference of experimental values in the present study and the values from AME2020. The yellow and green bars represent the error in the atomic mass as indicated in AME2020.

$$S_{2n} = -m(A, Z) + m(A - 2, Z) + 2m_n. \quad (3)$$

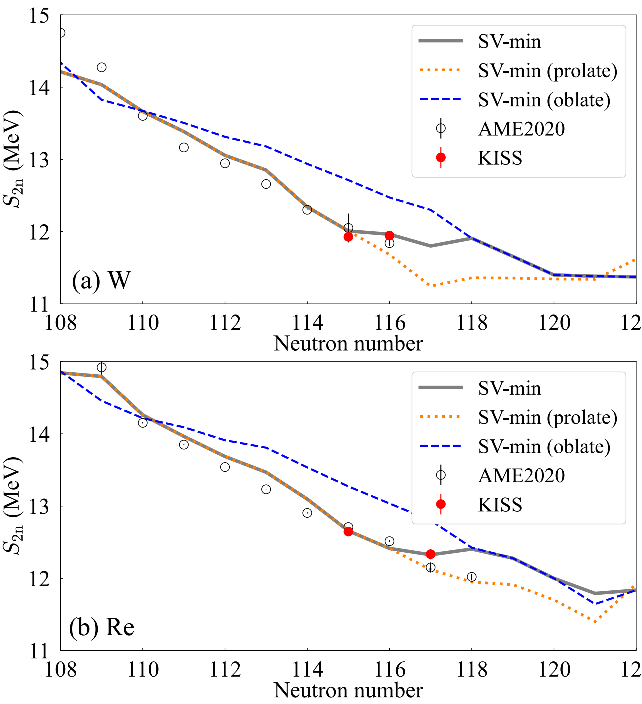

FIG. 4. Comparison of calculated and measured (or evaluated) two-neutron separation energies of W (a) and Re (b) isotopes. The calculation results with prolate and oblate shape constraints are shown by orange dotted and blue dashed lines, respectively, while calculations without shape constraints are shown by gray solid lines. Around the shape transition region, the gray line goes between the orange dotted and blue dashed lines. Experimental values shown by red circles were calculated using the measured mass values of ^{189,190}W and ^{188,190,192}Re at KISS.

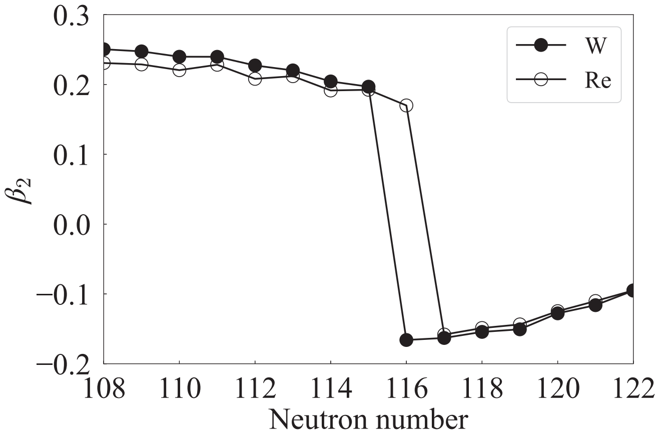

FIG. 5. Calculated quadrupole deformation parameters of W (closed circles) and Re (open circles) isotopes using axial Skyrme-Hartree-Fock-Bogoliubov calculations with the SV-min parametrization. A prolate-oblate shape transition occurs at the $N = 116$ isotope of W and the $N = 117$ isotope of Re.

Here, m_n represents the neutron mass. The mass value of ^{189}W, less bound than the extrapolated value in AME2020, results in a flattening trend of S_{2n} at ^{189,190}W. This trend has been reaffirmed through additional mass value verification in the present study. The trend is extensively discussed in Ref. [11], where it is suggested that the greater contribution of collective components in binding energy, based on the IBA model, is the reason for this trend in contrast to what is observed in Os isotopes. This interpretation is consistent with the explanation for the lower first 2^+ energy of W isotopes compared to Os isotopes.

The analyzed mass value of ^{192}Re deviates by approximately 2.6σ from the evaluated value in AME2020. The peak dominantly composed from Re ions so that Re ion yields are selectively enhanced by laser resonant ionization as shown in Fig. 2(b). The peak has been confirmed to be neither misattributed to nor biased by contaminant ions. For $A = 192$ isobars other than ^{192}Re, there were no significant deviations observed from the values in AME2020.

V. DISCUSSION

The two-neutron separation energy S_{2n} is an indicator of the binding strength of neutrons and generally decreases with increasing neutron number. In general, S_{2n} significantly decreases when the neutron number increases by one or two beyond a magic number, as observed in Figs. 1–9 of Ref. [8]. Outside the vicinity of magic-numbers, deviations from gradual decrease may appear due to localized changes in nuclear structure such as shape transition. In previous studies on Sr and Zr isotopes, similar to the present work, the trend of S_{2n} was shown to be partially flat or even increasing around shape transition regions [32]. The observed pattern in S_{2n} of W isotopes was interpreted using axial Skyrme-Hartree-Fock-Bogoliubov calculations [33] with the SV-min parametrization [34]. Figure 5 shows the calculated quadrupole deformation parameters of W and Re isotopes. It shows the shape transitions at $N = 116$ for W and $N = 117$ for Re, from a prolate shape in lighter nuclei to an oblate shape in heavier nuclei. Indeed, as shown in previous studies, such as Refs. [35–37], this transition is expected to occur through the triaxial degree of freedom. Because of the γ-soft character of the potential energy surface around ^{190}W, even if the true minimum were located at finite γ, the effect of restricting within the axial symmetry on S_{2n} would be expected to be small. In Figs. 4(a) and 4(b), the experimental and calculated S_{2n} values are combined in a single plot for the W and Re isotopes, respectively. The orange dotted and blue dashed lines show the calculation results obtained by taking the energy local minima in the prolate or oblate region, respectively, while the grey solid line shows the calculation results without such shape restriction. The experimental values were generally well reproduced by the unrestricted calculation results. As can be seen from the dashed lines, on the neutron-rich side above $N = 110$, there is a systematic tendency for the energy in the oblate shape to have a larger S_{2n} value than in the case of the prolate shape. The ^{189}W$_{115}$ (^{191}Re$_{116}$) case follows the S_{2n} systematics of the prolate deformation because ^{187,189}W (^{189,191}Re) are prolate in shape. On the other hand, S_{2n} of ^{190}W$_{116}$ (^{192}Re$_{117}$) deviates from the prolate systematics because ^{188}W (^{190}Re) has a prolate shape while ^{190}W (^{192}Re) has an oblate shape. The increase in S_{2n} of ^{190}W due to the shape transition creates a flat pattern in S_{2n} between ^{189}W and ^{190}W. On the other hand, the flat pattern seen between ^{189}W and ^{190}W was not observed in ^{191}Re and ^{192}Re. This is because the difference between the prolate and oblate energy minima in these Re isotopes is less than half of that in W, and the influence of the shape transition on S_{2n} is smaller in Re, as interpreted based on theoretical calculations. The experimental S_{2n} values up to $N = 117$ are well reproduced by the calculations, but the experimental value for ^{193}Re$_{118}$ deviates by about 0.5 MeV from the calculation without shape constraints. Additional experiments may reveal further insights.

VI. SUMMARY

In this study, a variety of nuclei were produced through multi-nucleon transfer reactions using a ^{136}Xe beam and a natural Ir target at the KISS facility. Subsequently, direct high-precision mass measurements were conducted using an MRTOF-MS with a mass resolving power of $m/\Delta m \approx 4 \times 10^5$. It confirmed previous determinations of the atomic mass of ^{189}W, which had been excluded from AME2020 due to a nonsmooth trend in S_{2n} at ^{189}W. Furthermore, the mass values for all measured nuclei, excluding ^{192}Re, agreed within 1σ with AME2020 values. The flat S_{2n} pattern between ^{189}W and ^{190}W, as well as the updated S_{2n} value for ^{192}Re, were interpreted as resulting from the shape transition at $N = 116$ for W isotopes and at $N = 117$ for Re isotopes, according to HFB calculations with the SV-min parametrization. At the KISS facility, we are advancing the development of a helium gas cell [38] to enhance the extraction yield of unstable nuclei. In the future, we anticipate reporting high-precision mass measurements for even more neutron-rich nuclei in the region of refractory elements around tungsten and the actinide region.

ACKNOWLEDGMENTS

The experiment was performed at the RI Beam Factory (RIBF) operated by RIKEN Nishina Center and CNS, University of Tokyo. The experiment was performed under Program No. NP2112-RRC72 at the RIBF. This work was supported by JSPS KAKENHI Grants No. JP23244060, No. JP24740180, No. JP26247044, No. JP15H02096, No. JP17H01132, No. JP17H06090, No. JP18H03711, No. JP20H00169, No. JP21H04479, No. JP22H00136, and No. JP23K13134. This work was partially supported by the JST ERATO (Grant No. JPMJER2304). M.M. acknowledges support from the RIKEN Special Postdoctoral Researchers (SPDR) program.

[1] M. R. Mumpower, R. Surman, G. C. McLaughlin, and A. Aprahamian, Prog. Part. Nucl. Phys. **86**, 86 (2016).
[2] X. Zhou *et al.*, Nat. Phys. **19**, 1091 (2023).
[3] P. Schury, K. Okada, S. Shchepunov, T. Sonoda, A. Takamine, M. Wada, H. Wollnik, and Y. Yamazaki, Eur. Phys. J. A **42**, 343 (2009).
[4] R. N. Wolf *et al.*, Int. J. Mass Spectrom. **349-350**, 123 (2013).
[5] S. Eliseev, K. Blaum, M. Block, C. Droese, M. Goncharov, E. Minaya Ramirez, D. A. Nesterenko, Yu. N. Nobikov, and L. Schweikhard, Phys. Rev. Lett. **110**, 082501 (2013).
[6] B. Franzke, H. Geissel, and G. Münzenberg, Mass Spectrom. Rev. **27**, 428 (2008).
[7] K. Blaum, Yu. N. Novikov, and G. Werth, Contemp. Phys. **51**, 149 (2010).
[8] M. Wang, W. J. Huang, F. G. Kondev, G. Audi, and S. Naimi, Chin. Phys. C **45**, 030003 (2021).
[9] M. Wang, G. Audi, F. G. Kondev, W. J. Huang, S. Naimi, and X. Xu, Chin. Phys. C **41**, 030003 (2017).
[10] P. Kauranen and H. Ihochi, J. Inorg. Nucl. Chem. **27**, 1451 (1965).
[11] D. Shubina *et al.*, Phys. Rev. C **88**, 024310 (2013).
[12] Y. Hirayama *et al.*, Nucl. Instrum. Methods Phys. Res., Sect. B **353**, 4 (2015).
[13] Y. Hirayama *et al.*, Nucl. Instrum. Methods Phys. Res., Sect. B **376**, 52 (2016).
[14] Y. Hirayama *et al.*, Nucl. Instrum. Methods Phys. Res., Sect. B **412**, 11 (2017).
[15] NIST Atomic Spectra Database Lines Data, https://physics.nist.gov/PhysRefData/ASD/lines_form.html
[16] Y. Hirayama *et al.*, Nucl. Instrum. Methods Phys. Res., Sect. B **463**, 425 (2020).
[17] T. Niwase *et al.*, Phys. Rev. Lett. **130**, 132502 (2023).
[18] J. Y. Moon *et al.*, RIKEN Accel. Prog. Rep. **52**, 138 (2019).
[19] Y. Ito, F. Arai, I. Katayama, P. Schury, T. Sonoda, M. Wada, and H. Wollnik, JPS Conf. Proc. **6**, 030112 (2015).
[20] P. Schury *et al.*, Nucl. Instrum. Methods Phys. Res., Sect. B **407**, 160 (2017).
[21] M. Wada *et al.*, Nucl. Instrum. Methods Phys. Res., Sect. B **204**, 570 (2003).
[22] F. Arai, Y. Ito, M. Wada, P. Schury, T. Sonoda, and H. Mita, JPS Conf. Proc. **6**, 030110 (2015).
[23] Y. Ito *et al.*, Nucl. Instrum. Methods Phys. Res., Sect. B **317**, 544 (2013).
[24] P. Schury *et al.*, Nucl. Instrum. Methods Phys. Res., Sect. B **317**, 537 (2013).
[25] P. Schury *et al.*, Rev. Sci. Instrum. **91**, 014702 (2020).
[26] Y. Ito *et al.*, Phys. Rev. C **88**, 011306(R) (2013).
[27] R. Brun and F. Rademakers, Nucl. Instrum. Methods Phys. Res., Sect. A **389**, 81 (1997), special issue, New Computing Techniques in Physics Research V.
[28] F. James and M. Roos, Comput. Phys. Commun. **10**, 343 (1975).
[29] T. D. Jhonson and B. Singh, Nucl. Data Sheets **142**, 1 (2017).
[30] B. Singh, Nucl. Data Sheets **99**, 275 (2003).
[31] C. M. Baglin, Nucl. Data Sheets **113**, 1871 (2012).
[32] R. Rodríguez-Guzmán, P. Sarriguren, L. M. Robledo, and S. Perez-Martin, Phys. Lett. B **691**, 202 (2010).
[33] M. V. Stoitsov, N. Schunck, M. Kortelainen, N. Michel, H. Nam, E. Olsen, J. Sarich, and S. Wild, Comput. Phys. Commun. **184**, 1592 (2013).
[34] P. Klüpfel, P.-G. Reinhard, T. J. Bürvenich, and J. A. Maruhn, Phys. Rev. C **79**, 034310 (2009).
[35] L. M. Robledo, R. Rodríguez-Guzmán, and P. Sarriguren, J. Phys. G: Nucl. Part. Phys. **36**, 115104 (2009).
[36] G. J. Lane *et al.*, Phys. Rev. C **82**, 051304(R) (2010).
[37] H. Watanabe *et al.*, Phys. Lett. B **814**, 136088 (2021).
[38] Y. Hirayama *et al.*, Nucl. Instrum. Methods Phys. Res., Sect. A **1058**, 168838 (2024).